

REPORT

CHEMICAL PHYSICS

Coherent imaging of an attosecond electron wave packet

D. M. Villeneuve,^{1,2*} Paul Hockett,¹ M. J. J. Vrakking,^{3,4} Hiromichi Niikura,^{5*}

Electrons detached from atoms or molecules by photoionization carry information about the quantum state from which they originate, as well as the continuum states into which they are released. Generally, the photoelectron momentum distribution is composed of a coherent sum of angular momentum components, each with an amplitude and phase. Here we show, by using photoionization of neon, that a train of attosecond pulses synchronized with an infrared laser field can be used to disentangle these angular momentum components. Two-color, two-photon ionization via a Stark-shifted intermediate state creates an almost pure f-wave with a magnetic quantum number of zero. Interference of the f-wave with a spherically symmetric s-wave provides a holographic reference that enables phase-resolved imaging of the f-wave.

In the Copenhagen interpretation of quantum mechanics, a particle is fully described by its complex wave function Ψ , which is characterized by both an amplitude and phase. However, only the square modulus of the wave function, $|\Psi|^2$, can be directly observed (1, 2). Recent developments in attosecond technology based on electron-ion recollision (3) have provided experimental tools for the imaging of the electronic wave function (not its square) in bound states or ionization continua. High-harmonic spectroscopy on aligned molecules was used to reconstruct the highest-occupied molecular orbital of nitrogen (4, 5) and to observe charge migration (6). Strong-field tunneling was used to measure the square modulus of the highest-occupied molecular orbital for selected molecules (7). Furthermore, recollision holography (8, 9) permitted a measurement of the phase and amplitude of a continuum electron generated in an intense laser field.

Complementary to recollision-based measurements, photoelectron spectroscopy with attosecond extreme ultraviolet (XUV) pulses has also measured photoelectron wave packets in continuum states (10–16) by exploiting quantum interferences (17–19). However, decomposition of the wave function of an ejected photoelectron into angular momentum eigenstates with a fully characterized amplitude and phase is more difficult. First, in general, a one-photon

transition with linearly polarized light generates two orbital angular momentum (ℓ) states, according to the selection rule $\Delta\ell = \pm 1$. Second, because the initial state has a $(2\ell + 1)$ -fold degeneracy (labeled by m , the magnetic quantum number) and because m is conserved for interactions with linearly polarized light, photoelectron waves with a range of m are produced. Hence, the photoelectron momentum distribution contains a sum of contributions from different initial states, each of which is a coherent sum of different angular momentum components, making it difficult to decompose the continuum state into individual angular momentum components (20–22).

Here we preferentially create an almost pure f-wave continuum wave function with $m = 0$ in neon by using an attosecond XUV pulse train synchronized with an infrared (IR) laser pulse through the process of high-harmonic generation. The isolation of the f-wave with $m = 0$ is attributed to the XUV excitation to a resonant bound state that is Stark-shifted by the IR field. By adding an additional coherent pathway that produces an isotropic electron wave, we create a hologram and reveal the alternating sign of the lobes of the f-wave. By controlling the phase of the interfering pathways with attosecond precision, we are able to determine the amplitudes and phases of all six partial-wave components that contribute to the continuum wave function.

The experimental setup is described in detail in the supplementary materials (SM). An 800-nm wavelength laser pulse with a 35-fs duration is focused onto an argon gas jet, producing high-harmonic emission that we label "XUV." In the frequency domain, the emission has peaks at odd-integer multiples of the driving laser frequency. In the time domain, the XUV pulse is composed of a train of attosecond pulses. The high-harmonic emission is focused onto a second gas jet con-

taining neon gas. The neon atoms are excited and photoionized by different high-harmonic orders, and the resulting photoelectrons are recorded by a velocity map-imaging (VMI) spectrometer, which measures their two-dimensional (2D) projection onto a detection plane (23). For the phase-resolved measurements, we generate an XUV spectrum that contains both even and odd harmonics, using both 800- and 400-nm driving laser pulses (24). In both cases, part of the 800-nm pulse (called "IR") is also focused onto the neon gas, permitting resonant $(1 + 1')$ -photon, XUV + IR ionization and Stark-shifting of the resonant bound states (25). The two-color temporal control and stability of the experiment is <50 as.

We first consider the situation where the XUV is generated by 800 nm only (i.e., no 400-nm contribution). The XUV spectrum then consists of a comb of odd harmonics of the IR driver laser frequency (i.e., no even harmonics). Figure 1A shows the XUV + IR photoelectron momentum distribution for the ionization of neon that is measured under these conditions. At very low momentum, i.e., close to the ionization threshold, a six-fold angular structure is clearly observed. For comparison, an image recorded for helium under the same conditions is shown in Fig. 1B. This experiment may be viewed as the angular-resolved version of a previous study in helium by Swoboda *et al.* (26), in which the phase shift due to an intermediate resonance was mapped out. For neon, in Fig. 1A, the outer ring is produced through direct ionization by harmonic 15 (H15), whereas the inner structure results from $(1 + 1')$ -photon, H13 + IR ionization through the 3d intermediate resonance. The widths in the radial direction of all observed features are a consequence of the frequency bandwidth of the XUV and IR pulses (27).

Figure 1C shows an energy level diagram that rationalizes the experimental observations in neon. The XUV photon energy and the IR intensity create a resonance condition for H13 with the Stark-shifted 3d level (see SM). The addition of an IR photon enables $(1 + 1')$ -photon ionization, producing the central feature seen in Fig. 1A. In Fig. 1C, the atomic eigenstates are labeled with the usual atomic physics notation, i.e., with principal quantum number n and with the orbital angular momentum labeled as s ($\ell = 0$), p ($\ell = 1$), d ($\ell = 2$), and f ($\ell = 3$). A dipole transition between states changes ℓ by ± 1 . For neon ($1s^2 2s^2 2p^6$), the $2p \rightarrow 3d$ transition is dipole-allowed, and in the dipole approximation, the continuum electron resulting from XUV + IR ionization must have either p- or f-wave character. We show that the experimental results are consistent with a continuum electron wave function that is predominantly an f-wave with $m = 0$.

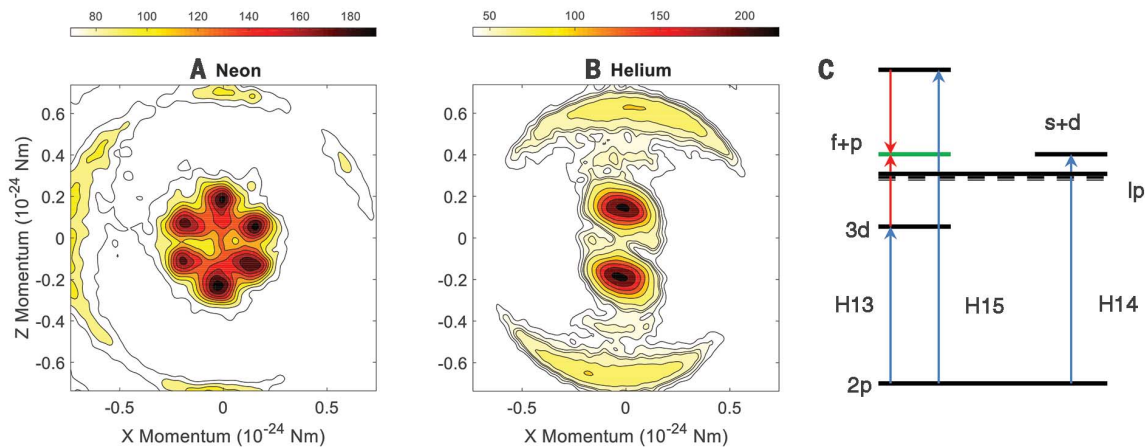
The amplitude of the six-fold structure is modulated when the relative delay between the XUV and the IR laser pulses is varied. This modulation is due to the interference between the resonant H13 + IR pathway and the nonresonant H15 – IR pathway (we use the notation H13 + IR and H15 – IR to denote two-photon pathways composed of one harmonic order plus or minus one infrared

¹National Research Council of Canada, 100 Sussex Drive, Ottawa, ON K1A 0R6, Canada. ²Joint Attosecond Science Laboratory, National Research Council and University of Ottawa, 100 Sussex Drive, Ottawa, ON K1A 0R6, Canada. ³Max-Born-Institut, Max-Born-Straße 2A, D-12489 Berlin, Germany. ⁴Fachbereich Physik, Freie Universität Berlin, Arnimallee 14, 14195 Berlin, Germany.

⁵Department of Applied Physics, Waseda University, Okubo 3-4-1, Shinjuku, Tokyo 169-8555, Japan.

*Corresponding author. Email: david.villeneuve@uottawa.ca (D.M.V.); niikura@waseda.jp (H.N.)

Fig. 1. Experimental velocity-map electron images. The observed photoelectron momentum distributions result from the ionization of (A) neon and (B) helium by an attosecond pulse train synchronized with the fundamental IR laser pulse. Both pulses were polarized along the vertical (z) axis. In both images, the outer rings are due to direct ionization by harmonics 15 (neon) and 17 (helium). The central feature in the neon image results from $(1 + 1')$ -photon, XUV + IR ionization via the 3d state. The slight left-right asymmetry arises from imperfections in the microchannel plate detector. An energy level diagram in (C) shows the levels that are relevant for understanding the neon experiment. The green line labels the six-fold low-energy feature seen in (A).



photon). The SM shows that the phase of the six-fold structure is different from that of the higher-order sidebands, consistent with the occurrence of a phase shift due to the 3d resonance. This result is consistent with the observations of Swoboda *et al.* (26) in helium.

Experimentally, the resonant excitation to the Stark-shifted 3d state can be confirmed by measurements of the photoelectron momentum distribution as a function of both the photon energy of the XUV and the IR laser intensity (0 to 4×10^{12} W/cm 2 ; see SM). At a given XUV photon energy, the six-fold structure is observed when the H13 photon energy matches the 2p \rightarrow 3d resonant energy plus the ponderomotive shift resulting from the IR laser intensity (see SM). However, when the XUV photon energy is larger than the Stark-shifted 2p \rightarrow 3d transition, the six-fold structure disappears into a broad distribution.

The initial 2p state of neon has three orthogonal orbitals, p_x , p_y , and p_z (we consider that in the experiment the laser is polarized along the z direction, and the photoelectron is detected in the xz plane). Ionization from each initial state should contribute to the final angular distributions. The three components of a continuum f-wave resulting from $(1+1')$ -photon ionization from the three p orbitals are illustrated in Fig. 2, along with their simulated VMI projections. It is clear that the six-fold structure of Fig. 1A corresponds only to the $m = 0$ case, which is the only orbital that displays the experimentally observed node in the horizontal direction (x direction). The dominance of the $m = 0$ channel is both notable and unexpected. Like the ground state, in the absence of the laser field, the $m = 0$ and $m = \pm 1$ components of the 3d resonance are degenerate. Our experiment thus suggests that a Stark shift of the 3d resonant state may be responsible for the selection of the $m = 0$ component. We show in the SM that the Stark shift and ionization rate may be different for $m = 0$ and $m = \pm 1$, causing only

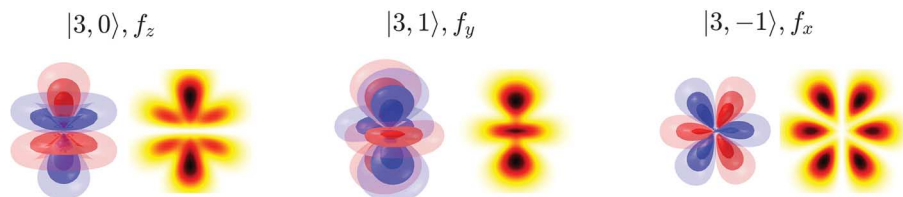


Fig. 2. Calculated continuum wave functions and predicted VMI projections. The individual wave functions for the possible f-wave components are shown to the left of the corresponding projections of the square of the wave function on a 2D plane. Quantization axis is along the vertical (z) axis. Only the $m = 0$ case (left) is consistent with the experiment, which always exhibits a node along the horizontal axis. The radial part of the wave functions was simulated with a Gaussian width to correspond to the experimental energy width of the VMI images; the radial information in the experiment is not used—only the angular distributions are used. $f_y = \text{Im}(|3,1\rangle + |3,-1\rangle)/\sqrt{2}$ and $f_x = \text{Re}(|3,1\rangle - |3,-1\rangle)/\sqrt{2}$.

the $m = 0$ channel to be shifted into resonance. Figure S5 shows that, for a particular combination of XUV frequency and IR intensity, the contribution of photoelectrons produced through the $m = 0$ channel exceeds by an order of magnitude the contributions from the $m = \pm 1$ channels. This calculation was performed with a 3D time-dependent Schrödinger equation (TDSE) solver by using an effective potential for argon, not neon. As discussed in the SM, this calculation demonstrates the plausibility of $m = 0$ selection by the Stark shift, but the calculation must be done for a benchmarked neon potential.

We next modified the experiment by introducing a third, XUV-only, one-photon pathway to the final continuum state as a homodyne phase reference. Experimentally, this was done by adding the second harmonic of the 800-nm laser pulse to the high-harmonic generation process, resulting in the creation of both even and odd harmonics (24). Even-order harmonic H14 creates photoelectrons with the same energy as the H13 + IR and H15 - IR pathways (see Fig. 1C). Direct

ionization from the 2p ground state by H14 produces s- and d-waves, which interfere with the predominant f-wave that is created by both $(1 + 1')$ -photon processes. By varying the relative delay between the XUV and IR pulses, the phases of the XUV + IR, $(1 + 1')$ -photon processes are altered, whereas the s- and d-waves are unaffected by the delay, providing a constant phase reference for the other channels.

Figure 3 shows measured photoelectron momentum distributions from neon at three different XUV-IR time delays. Compared with Fig. 1A, the lobes in the six-fold angular pattern alternate in intensity, and the intensity distribution is controlled by the XUV-IR delay. The alternating three-fold features can be rationalized in a simple picture by coherently adding an f-wave to an s-wave, or taking their difference, as illustrated in Fig. 3, while neglecting the p- and d-wave components.

The three VMI images shown in Fig. 3A are taken from a series of 100 images recorded at different XUV-IR time delays. These images were

binned into 8° angular sectors, and the counts in each sector were integrated to extract the angular distribution for each image. In Fig. 4A, we plot the observed electron angular distributions of the

central structure as a function of the XUV-IR delay. The experimental results are compared to a model in which six possible spherical harmonics are added coherently and then projected

onto the xz plane to simulate the VMI images. The total continuum wave function is written as

$$\begin{aligned} \psi(\theta, \phi) = & A_s Y_{00} + A_d e^{i\phi_d} Y_{20} + \\ & (A_{p13} e^{i\phi_{p13}} Y_{10} + A_{f13} e^{i\phi_{f13}} Y_{30}) e^{i\omega_0 \tau} + \\ & (A_{p15} e^{i\phi_{p15}} Y_{10} + A_{f15} e^{i\phi_{f15}} Y_{30}) e^{-i\omega_0 \tau} \end{aligned} \quad (1)$$

where the A 's represent amplitudes of each partial wave contribution, ϕ are the corresponding phases, ω is the IR laser frequency, τ is the XUV-IR delay time, and $Y_{\ell m}(\theta, \phi)$ are spherical harmonics. The first two terms of the right side of the equation describe the one-photon ionization by H14 producing s- and d-waves, whereas the latter two terms (containing the dependence on the XUV-IR delay τ) result from the pathway through the 3d resonant state involving H13, and the direct ionization channel involving H15, both producing p- and f-waves. A fit of this model to the experimental data yields the results shown in Fig. 4B; the fitting parameters are listed in Table 1. To ensure that a global optimum was found, we employed a particle swarm optimization algorithm with 10^7 initial conditions. The amplitudes in Table 1 confirm the dominance of the f- and s-wave components over the respective p- and d-wave components that we have used in the discussion of Fig. 3.

As an additional check, we show in the SM that the partial-wave amplitudes and phases in Table 1 are consistent with several further experiments. One is the series of experiments that produced the data shown in Fig. 1A, which were recorded without H14 present; here the equal intensities of all six lobes can only be reproduced when the f- and p-waves are added with the relative phase and amplitude shown in Table 1. In a

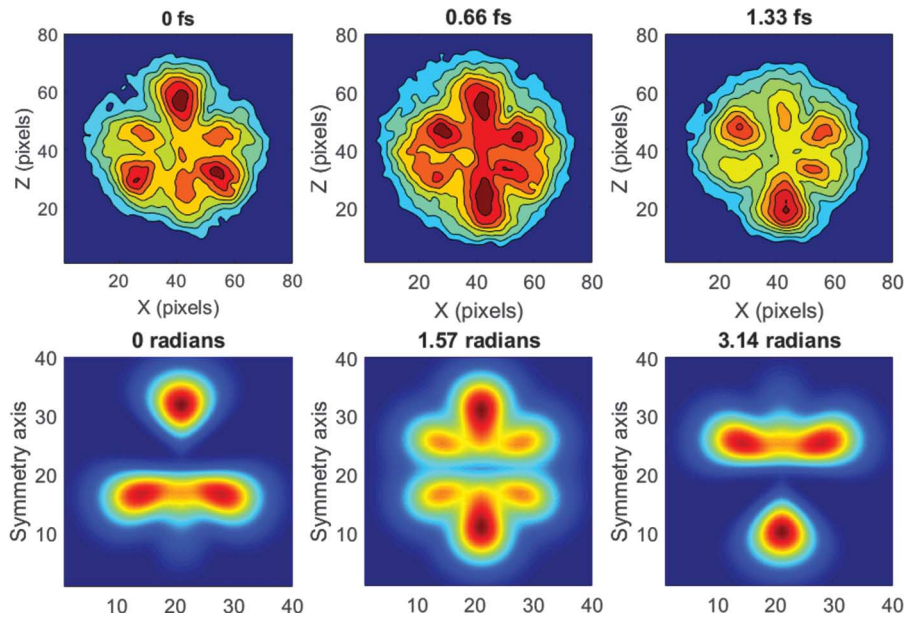


Fig. 3. Electron momentum angular distributions with three pathways. (Top) Experimental electron momentum distributions resulting from the ionization of neon via the three pathways (H13, H14, H15) shown in Fig. 1C. The polarization direction is vertical. (Bottom) Calculated images for a pure s-wave added to a pure f-wave ($m = 0$) with equal amplitudes, squared and projected onto a plane, to show that the experimental results are dominated by these two components. For simplicity (and as supported by the data in Table 1), the p- and d-wave contributions are not included. The s-wave component is produced by direct one-photon ionization with H14 and provides a phase reference for the other two interfering pathways. As the phase of the IR pulse is advanced by the times shown above each figure, the phase of the f-wave component is varied. The resulting interference introduces an up-down asymmetry in the momentum distribution that can be controlled by the IR phase.

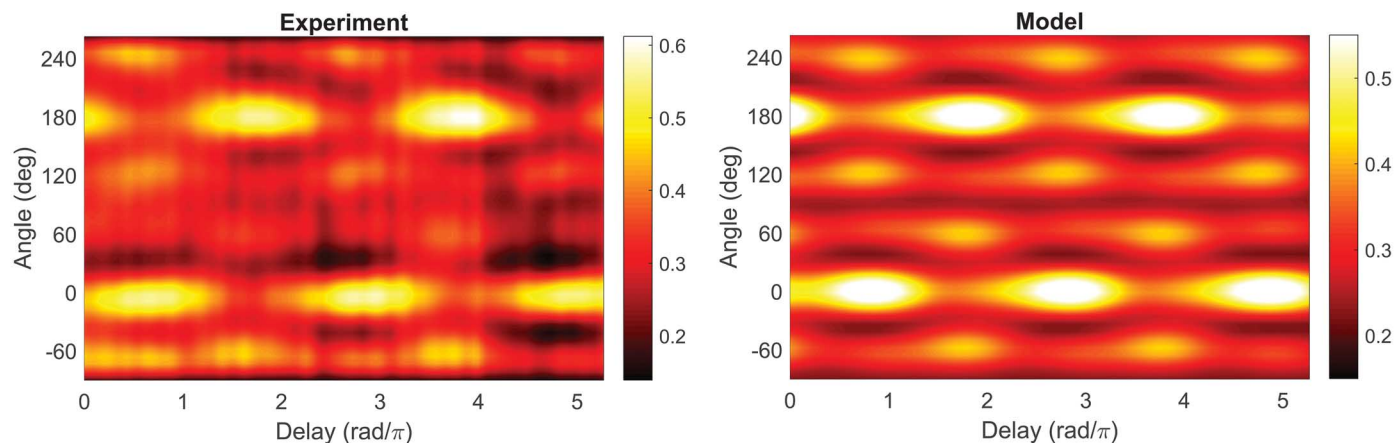


Fig. 4. Angular distribution of the central feature of the VMI images versus XUV-IR delay. Angle zero is defined as the upward direction in the VMI images, parallel to the polarization (z) axis. A delay of π radians corresponds to a delay of half an IR optical period (1.33 fs). (Left) Experimental data. (Right) Calculated angular distribution based on fitting a 12-parameter model (see Eq. 1) to the experimental data. The amplitudes and phases of each partial wave are listed in Table 1. The dominant pattern is reproduced: Alternating lobes at 0° and 180°, with minor lobes at -60°, 60°, 120°, and 240°. This pattern is associated with the six-fold structure of the dominant f-wave contribution.

Table 1. Parameters of the model fit. The experimental photoelectron angular distributions as a function of XUV-IR delay, shown in Fig. 4A, are fitted to a model composed of six partial waves (see Eq. 1). The amplitudes and phases of each partial wave are listed. The amplitudes are normalized so that the sum of their squares equals one. The phase of the s-wave is defined as zero. ϕ_0 represents an arbitrary common phase that determines time zero. The column labeled “Amplitude²” is the square of the values in the “Amplitude” column. Errors shown are the range of each parameter such that the residual least-squares error between the model and the experiment increases by 10%.

Fitting parameter	Amplitude	Amplitude ²	Phase (rad)
A_s	$0.83^{+0.04}_{-0.04}$	0.697	0
A_{p13}	$0.16^{+0.05}_{-0.05}$	0.024	$0.54^{+0.41}_{-0.34} + \phi_0$
A_{p15}	$0.15^{+0.05}_{-0.04}$	0.022	$1.93^{+0.41}_{-0.42} - \phi_0$
A_d	$0.10^{+0.05}_{-0.06}$	0.011	$1.57^{+0.30}_{-0.30}$
A_{f13}	$0.32^{+0.04}_{-0.04}$	0.104	$4.16^{+0.19}_{-0.20} + \phi_0$
A_{f15}	$0.39^{+0.03}_{-0.04}$	0.151	$5.04^{+0.16}_{-0.16} - \phi_0$

further experiment, no IR was present, and the inner structure was produced by H14 alone; here the observed angular distribution is in approximate agreement with the relative phase and amplitude of the s- and d-waves in Table 1.

We have shown that, by combining coherent photoionization pathways through a Stark-shifted resonant state, we can create almost pure f-waves with a single magnetic quantum number $m = 0$. The addition of a direct photoionization pathway producing predominantly an s-wave provides a constant phase reference that allows a determination of the phase of the f-wave lobes. By varying the relative phase of the pathways, we can control the direction in which the electrons emanate from the atom, and we can verify the quantum phase of the lobes of the f-wave. We have spatially imaged the angular structure of the continuum wave function and coherently interfered it using a holographic reference composed largely of an isotropic s-wave, leading to the determination of the sign of the quantum wave function. This is a form of coherent control, in which the parity and direction of the electrons can be controlled (13, 19).

In addition, the fitting of a model to the complete experimental data set allows us to deter-

mine the exact makeup of the total continuum wave function. In particular, we can determine the amplitude and phase of each partial-wave component. In photoionization parlance, this is a “complete” experiment (20).

We have implemented a number of novel approaches, such as a sophisticated two-color interference experiment with careful use of both even and odd harmonics and the use of Stark-tuning to include or exclude desired quantum pathways. These new tools in the attosecond toolbox may allow us to study more complex systems. For example, can we apply a similar approach to a molecule? By exploiting rotational wave packets, will it be possible to determine both the amplitude and phase of transition moments in the molecular frame?

If the photon energy of the XUV can be tuned widely to select a particular intermediate quantum state, our method allows the measurement of phase-resolved orbital images of other states and in different atoms. For instance, if the electron is excited from a lower-lying level to a doubly excited state, dynamical changes in the amplitude and phase resulting from electron correlation can be imaged directly with attosecond time resolution.

REFERENCES AND NOTES

1. H. Wimmel, *Quantum Physics and Observed Reality: A Critical Interpretation of Quantum Mechanics* (World Scientific, Singapore, 1992).
2. A. S. Stodolska et al., *Phys. Rev. Lett.* **110**, 213001 (2013).
3. H. Niikura et al., *Nature* **417**, 917–922 (2002).
4. J. Itatani et al., *Nature* **432**, 867–871 (2004).
5. S. Haessler et al., *Nat. Phys.* **6**, 200–206 (2010).
6. P. M. Kraus et al., *Science* **350**, 790–795 (2015).
7. M. Meckel et al., *Science* **320**, 1478–1482 (2008).
8. M. Meckel et al., *Nat. Phys.* **10**, 594–600 (2014).
9. D. Ray et al., *Phys. Rev. Lett.* **100**, 143002 (2008).
10. V. Gruson et al., *Science* **354**, 734–738 (2016).
11. S. Haessler et al., *Phys. Rev. A* **80**, 011404 (2009).
12. K. T. Kim et al., *Phys. Rev. Lett.* **108**, 093001 (2012).
13. G. Laurent et al., *Phys. Rev. Lett.* **109**, 083001 (2012).
14. J. Mauritsson et al., *Phys. Rev. Lett.* **105**, 053001 (2010).
15. T. Remetter et al., *Nat. Phys.* **2**, 323–326 (2006).
16. A. Rouzée et al., *J. Phys. At. Mol. Opt. Phys.* **47**, 124017 (2014).
17. J. Cooper, R. N. Zare, *J. Chem. Phys.* **48**, 942–943 (1968).
18. J. Cooper, R. N. Zare, in *Atomic Collision Processes*, G. Gelman, K. T. Mahanthappa, W. E. Brittin, Eds. (Lectures in Theoretical Physics, Gordon and Breach, 1969), vol. XIc, pp. 317–337.
19. Y.-Y. Yin, C. Chen, D. S. Elliott, A. V. Smith, *Phys. Rev. Lett.* **69**, 2353–2356 (1992).
20. U. Becker, *J. Electron Spectrosc. Relat. Phenom.* **96**, 105–115 (1998).
21. J. C. Hansen, J. A. Duncanson, R.-L. Chien, R. S. Berry, *Phys. Rev. A* **21**, 222–233 (1980).
22. K. L. Reid, *Annu. Rev. Phys. Chem.* **54**, 397–424 (2003).
23. A. T. J. B. Eppink, D. H. Parker, *Rev. Sci. Instrum.* **68**, 3477–3484 (1997).
24. N. Dudovich et al., *Nat. Phys.* **2**, 781–786 (2006).
25. E. B. Salomon, C. J. Sansonetti, *J. Phys. Chem. Ref. Data* **33**, 1113–1158 (2004).
26. M. Swoboda et al., *Phys. Rev. Lett.* **104**, 103003 (2010).
27. N. Dudovich, D. Oron, Y. Silberberg, *Phys. Rev. Lett.* **88**, 123004 (2002).

ACKNOWLEDGMENTS

The authors gratefully acknowledge discussions with T. Morishita, A. Stolow, M. Ivanov, I. Tamblyn, and A. Korobenko, as well as funding from the Japan Society for the Promotion of Science (JSPS) Grants-in-Aid for Scientific Research (KAKENHI) grant no. 25247069. Data are available upon request from david.villeneuve@uottawa.ca.

SUPPLEMENTARY MATERIALS

www.sciencemag.org/content/356/6343/1150/suppl/DC1
Materials and Methods
Figs. S1 to S8
Table S1
References (28–32)
23 January 2017; accepted 3 May 2017
10.1126/science.aam8393

PHYSICS

Tracking the dynamics of electron expulsion

Electron holography is used to map out the wave function of a photo-emitted electron

By Caterina Vozzi

Since the birth of quantum mechanics, scientists have been dreaming of imaging, and possibly controlling, the motion of electrons in atoms and molecules. These electrons are described in the quantum theory by wave functions. However, the wave function is an elusive quantity: It is a complex function with an amplitude and phase, but its square modulus is usually the only quantity directly measurable in experiments. In addition, visualizing the electron dynamics requires extremely high temporal resolution, on the order of attoseconds ($1 \text{ as} = 10^{-18} \text{ s}$). On page 1150 of this issue, Villeneuve *et al.* (1) report on an elegant experiment that demonstrates the possibility of fully reconstructing the electron wave function in the photoionization of neon and thus paving the way for coherent control of the process.

The description of the interaction between light and atoms at the atomic scale, which is the quintessence of quantum mechanics, has received a strong push in recent years due to the development of attosecond technology. The main goal of attosecond science is the realization of time-resolved experiments for imaging and possibly controlling the electron dynamics in atoms and molecules. These experiments have allowed the visualization of extremely fast dynamics (2–4). In this framework, photoionization is the simplest experiment that grants access to information about the wave function of an electron escaping from an atom. Despite the extensive effort dedicated to the study of photoionization, questions still need to be fully addressed, such as what is the influence of electron correlation in the photoionization dynamics (5).

The wave function of a particular electronic state can be written as the sum of an-

gular momentum components. One of the key aspects in photoionization experiments is the full reconstruction of this decomposition for the freed electron in amplitude and phase. Villeneuve *et al.* implemented a holographic approach for the full reconstruction of the electron wave function. In optical holography, information about the phase, which corresponds to the three-dimensionality of the object, is recorded in a two-dimensional (2D) image as an intensity modulation. This modulation is due to the interference between the light coming from the object and a reference beam. In the same way, the reconstruction of the electron angular momentum components can be inferred from the interference between different ionization pathways lead-

be recorded by a velocity map imaging spectrometer as a function of the delay between the XUV pulse train and the IR pulse. Each 2D electron momentum spectrum is an image of the electron wave function. The idea is simple and smart: The phase of the two interfering wave functions can be controlled with attosecond precision by changing the delay between the XUV and the IR pulse, and the angular momentum components of the electron wave function can be fully reconstructed in amplitude and phase, exploiting a simple fit with spherical harmonic functions.

The manipulation of the electric field at petahertz frequency allows the steering of the electron in a specific electronic state and the possibility to use interferometric techniques for visualizing this state. The strengths of this approach are the relative ease of the experiment and the need of a relatively simple theoretical model for the interpretation of the results. Its flexibility relies on the possibility of tuning the XUV photon energy in the attosecond pulse train for resonantly matching transition energies in different kind of atoms and molecules.

Over the past 15 years, several experimental approaches have been developed in strong-field physics and attosecond science for the visualization of atomic and molecular wave functions and their dynamics with impressive results (7, 8). This further piece of the puzzle represents indeed a very exciting finding for fundamental research in atomic physics. However, we can also foresee more visionary applications of the proposed method. These results may lead, for example, to the realization of full coherent control of photoionization, not only in atoms, but also in molecular systems, with the possibility to exploit attosecond pulse trains to steer the outcome of a chemical reaction or to select a particular dissociation path after the photoionization of molecules.

How far will it be possible to extend this picture, and how complex can the reconstructed quantum wave functions be? The answers constitute the boundaries of attosecond science that need to be investigated in the future. ■

REFERENCES

1. D. Villeneuve *et al.*, *Science* **356**, 1150 (2017).
2. F. Calegaro *et al.*, *Science* **346**, 336 (2014).
3. X. Xie *et al.*, *Phys. Rev. X* **4**, 021005 (2014).
4. P.M. Kraus *et al.*, *Science* **350**, 790 (2015).
5. M. Ossiander *et al.*, *Nat. Phys.* **13**, 280 (2017).
6. M. Swoboda *et al.*, *Phys. Rev. Lett.* **104**, 103003 (2010).
7. J. Itatani *et al.*, *Nature* **432**, 867 (2004).
8. D. Shafir *et al.*, *Nature* **485**, 343 (2012).

10.1126/science.aan5213

Institute for Photonics and Nanotechnologies, CNR, Milan, Italy. Email: caterina.vozzi@cnr.it

Supplementary Materials for **Coherent imaging of an attosecond electron wave packet**

D. M. Villeneuve,* Paul Hockett, M. J. J. Vrakking, Hiromichi Niikura*

*Corresponding author. Email: david.villeneuve@uottawa.ca (D.M.V.); niikura@waseda.jp (H.N.)

Published 16 June 2017, *Science* **356**, 1150 (2017)
DOI: 10.1126/science.aam8393

This PDF file includes:

- Materials and Methods
- Figs. S1 to S8
- Table S1
- References

1. Experimental set-up

The optical set-up for the two-color attosecond experiments employs a collinear arrangement for the two colors to keep relative timing jitter to less than 50 attoseconds. We use a commercially available Ti:sapphire amplifier system (Komodo-Dragon, KMLabs) to generate a 5.7 mJ, 1 kHz, ~790 nm laser pulse. After attenuating down to ~2mJ/pulse, we divide the pulse spatially and temporally by inserting a 1 mm thickness fused silica plate, covering the upper 70% of the beam, into the incident beam before the focusing element. The IR pulse transmitted through the fused silica plate, referred to as the driving laser pulse and delayed by 3 ps, is used for the generation of high-harmonics, while the other IR pulse is used as the perturbing field. We generate high-harmonics by focusing both pulses into a pulsed argon gas jet. After producing the high-harmonics, the driving IR laser pulse is eliminated by two silicon mirrors, whereas the probing IR pulse is reflected by a silver surface coated on the upper part of the silicon mirrors. We focus both high-harmonics beams and the probe laser pulse by a 540 mm focal length, gold coated toroidal mirror into a second pulsed gas jet containing neon or helium gas. In order to compensate and adjust the delay between the high-harmonic beam and the probing IR pulse, we insert another fused silica plate in the optical path of the probing IR pulse.

We use a standard, velocity map imaging apparatus [23] which consists of three electrodes and a micro-channel plate (MCP) with a diameter of 70 mm. The photoionized electrons are accelerated by the electrodes to the MCP. The photoelectron image is monitored by a CCD camera and transferred to a computer. The polarization axis of the 800 nm pulse (Z-axis) was kept horizontal in the VMI, i.e. perpendicular to the acceleration axis (Y-axis). The intensity of the IR was confirmed not to generate any ATI electrons, by turning off the HHG gas jet.

In order to generate both odd and even harmonic orders, a 400-nm pulse is generated collinear with the 800-nm pulse by a β -BBO crystal [24]. The delay between the 800 and 400-nm pulses is adjusted by a calcite plate so that both pulses are overlapped temporally in the region where the high-harmonics are generated. The polarization direction of the 800-nm and 400-nm are approximately parallel. In the images presented here, it was possible that the 400-nm polarization was not exactly parallel to the 800-nm polarization, possibly resulting in H14 having a small elliptical component. To rule this out, we have repeated the experiment with 400 and 800-nm polarizations exactly parallel, confirming that equivalent angular distributions (and their time-dependent feature) are obtained. The APT that follows the same second beam path is removed by a second fused silica plate before the VMI, which also balances the path length between the two beam paths. The relative delay

between the two beam paths is controlled by rotating the fused silica plate.

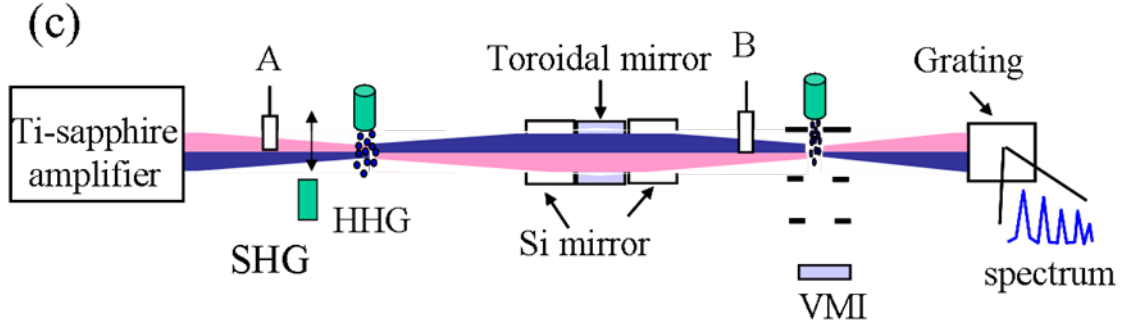


Figure S1. Experimental setup. The 800-nm output of the Ti;Sa laser is focused into a pulsed gas jet of argon. An attosecond pulse train is emitted from the gas jet, collinear with the 800-nm pulse. The APT is focused with a toroidal mirror into a second gas jet of neon, inside a velocity map imaging photoelectron spectrometer. The 800-nm pulse is removed from the APT by using a pair of silicon mirrors. In the VMI, the photoelectrons are accelerated by an electric field to the MCP detector and recorded by a CCD camera. To provide the infrared dressing field in the VMI, a parallel beam path is provided for 30% of the incident beam. After passing through the argon gas jet, the second beam is reflected from the portion of the silicon mirrors that is coated with silver, and transmitted through an iris. The APT that follows the same second beam path is removed by a second fused silica plate before the VMI, which also balances the path length between the two beam paths. The relative delay between the two beam paths is controlled by rotating the fused silica plate.

2. The photon energy and IR intensity dependence of the photoelectron momentum distribution.

In this section, we present our supplemental experimental results, showing that the Stark shift is responsible for the appearance of the six-fold structure (f-orbital) in the photoelectron momentum distribution. To do this, we independently control the frequency of the high order harmonics (by slightly tuning the 800-nm central wavelength, thereby precisely controlling the photon energy of H13), and the intensity of the probing IR pulse. We find that the f-orbital appears in a particular range of the IR intensity and photon energy. Outside of this range, a broad structure appears. We confirm that the 6-fold structure involves a resonant state by measuring the APT-IR delay dependence of the photoelectron momentum distribution.

2-1. The IR laser intensity dependence.

Fig. S2 shows velocity map electron momentum images at various probing IR laser intensities of (a) $0 \times 10^{12} \text{ W/cm}^2$ (i.e. only APT), (b) $0.5 \times 10^{12} \text{ W/cm}^2$, (c) $2.0 \times 10^{12} \text{ W/cm}^2$, and (d) $4.0 \times 10^{12} \text{ W/cm}^2$, respectively. The 13th harmonic photon energy corresponds to 20.24 eV. The polarization direction of both pulses is vertical in the figure.

As seen in Fig. S2, the appearance of the six-fold structure depends on the IR laser intensity. Without the IR field, no structure is recognized in the center region, whereas the broad ring structure appears at an intensity of $0.5 \times 10^{12} \text{ W/cm}^2$, and the six-fold structure appears for intensities larger than $1.7 \times 10^{12} \text{ W/cm}^2$ (not shown). As the IR intensity is increased further, the radius of the six-fold structure decreases. This indicates that the appearance of the six-fold structure can be attributed to a Stark effect: if the ionization would take place by an XUV+IR two-photon process without involvement of the Stark effect, then the radial distribution of the ejected photoelectron would remain the same and only the signal counts would increase as the IR laser intensity increases. The Stark shift is also evident in the decreasing electron kinetic energy in the outer photoelectron ring that is produced by 15th harmonic ionization.

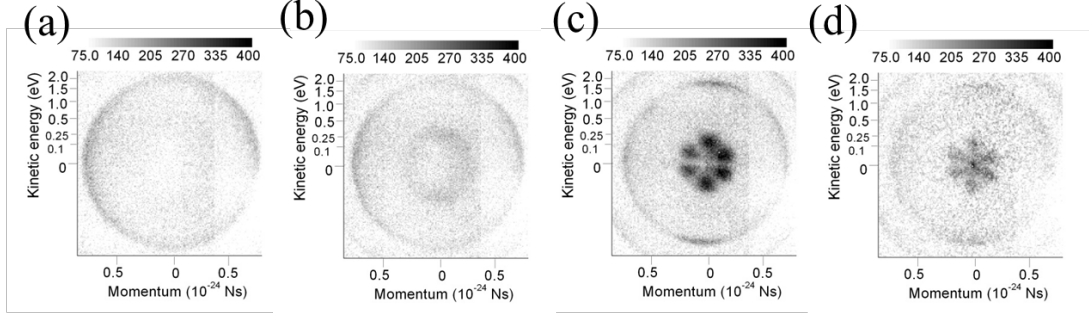


Fig. S2. The IR intensity dependence of the observed photoelectron momentum distribution of neon. The 13th harmonic photon energy is 20.24 eV. The IR intensity is (a) 0, (b) 0.5, (c) 2.0, and (d) 4.0×10^{12} W/cm², respectively.

As the simplest approximation, we assume that both the IP and the resonant state energy increase linearly with the ponderomotive energy shift, U_p , as the IR intensity increases. (Rydberg states will shift upward by the ponderomotive energy, which gives an upper limit for the ponderomotive shift of the 3d state.) With this assumption, the 2p-3d transition energy under the influence of the IR field is estimated by $E_{3d} = U_p + 20.04$ eV, where 20.04 eV is the field-free 2p-3d transition energy. The calculated U_p and E_{3d} are summarized in Table S1.

This simple model is consistent with the prediction that the six-fold structure appears via the 3d resonant state in the presence of the IR field, and accounts for the variation of the center structure as a function of the IR intensity shown in Fig. S2. At the lower IR intensity, the 13th harmonic energy (20.24 eV) is larger than the estimated 3d resonant energy (E_{3d}), and photoelectron rings associated with non-resonant transition are observed. When the 13th harmonic energy is almost coincident with the Stark-shifted E_{3d} , then the six-fold structure appears. Table S1 shows the estimated Stark-shifted energy of the 2p-3d transition as a function of IR intensity, based on this simple model. The IR intensity which gives the well-defined f-wave in Fig. S2 coincides with the intensity that shifts the 2p-3d transition into resonance with H13.

	I (10^{12} W/cm 2)	Up (eV)	E _{3d} (eV)
(a)	~0	~0	20.04 eV
(b)	0.5	0.03	20.07 eV
(c)	2.0	0.12	20.16 eV
(d)	4.0	0.24	20.28 eV

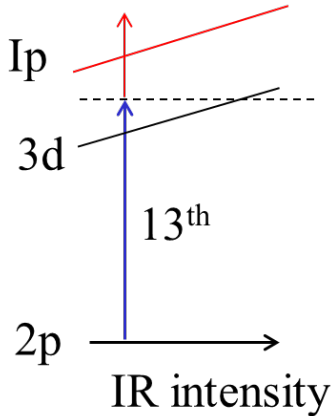


Table S1. The estimated ponderomotive shift (Up) and the 3d resonant state (E_{3d}) in the IR field as a function of the IR laser intensity. The right panel illustrates how the energy levels are Stark-shifted into resonance with H13 by the IR laser field.

2-2. The 13th harmonic photon energy dependence.

The exact frequency of H13 can be controlled by slightly shifting the central frequency of the Ti:Sa laser. The actual frequency can be accurately measured by recording the photoelectron energies from all harmonic orders above the Ip of neon and extrapolating to the Ip, in the absence of the IR field. We recorded photoelectron images as a function of the photon energy of H13 at a fixed IR laser intensity of 1.3×10^{12} W/cm 2 . The results are shown in Fig. S3. As the energy of H13 is increased from 20.06 eV to 20.38 eV, the radius of the six-fold structure increases, and then becomes a broad structure as H13 reaches 20.38 eV. The photon energy range where the six-fold structure appears is near the 2p-3d resonance energy in the presence of the IR field, estimated at 20.12 eV.

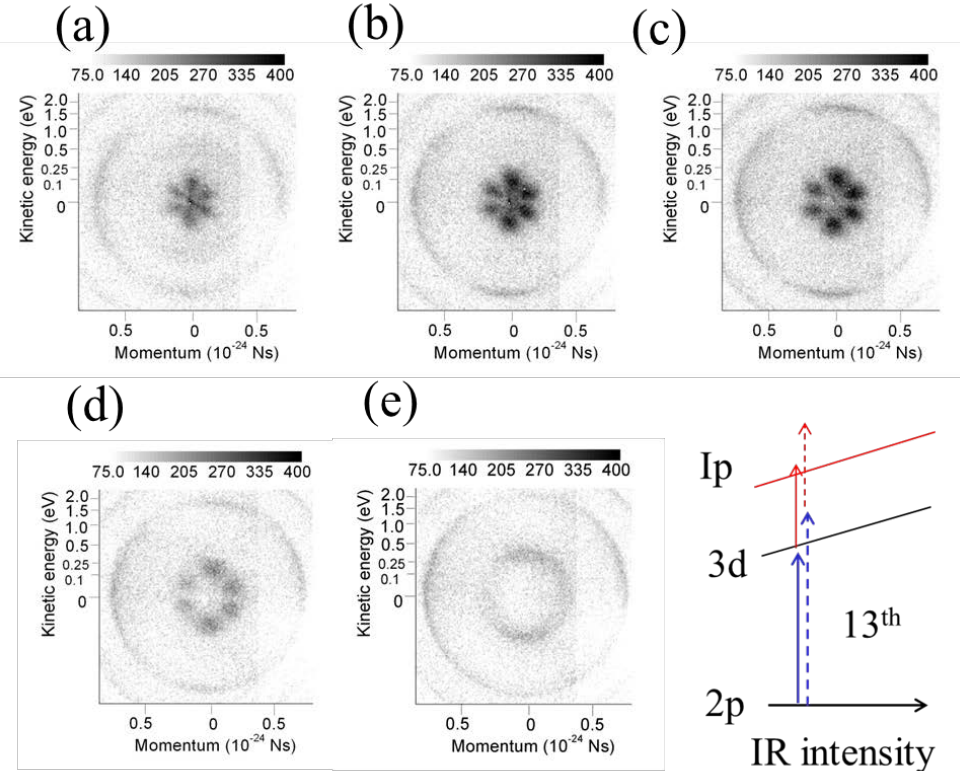


Fig. S3. Velocity map images of neon as a function of the photon energy of H13. The 13th harmonic energy is (a) 20.06 eV, (b) 20.10 eV, (c) 20.16 eV, (d) 20.24 eV, and (e) 20.38 eV, respectively. We also illustrate the energy diagram and excitation paths schematically. The 2p-3d transition can be brought into resonance with H13 either by changing the frequency of H13, or by Stark-shifting the 3d level with the IR intensity.

2-3. APT-IR delay dependence.

So far, we have shown that the six-fold structure appears when the 13th harmonic energy is close to the Stark-shifted 3d energy, whereas a broad angular distribution is observed when the photon energy is larger than that. Here we confirm that the resonant transition is involved in the appearance of the six-fold structure by measuring the APT-IR delay dependence of the photoelectron momentum distribution. This is done for the case where an 800-nm-only driving laser was used, i.e. in the absence of even harmonic orders.

Fig. S4 shows the measured intensity modulation for the photoelectron peaks as a function of the APT-IR delay for the case where (a) a broad distribution and (b)

a six-fold structure appear, respectively. The lowest panel for each figure shows the integrated signal counts of the center structure, labeled as A, whereas the higher panels are RABBIT sidebands [28,29].

The photoelectron signal modulation of feature A is caused by the interference between two ionization pathways. Pathway 1 is ionization by H13+IR through the 3d state. Pathway 2 is ionization by H15-IR, i.e. direct ionization to the continuum via H15 accompanied by stimulated emission of one IR photon. The pure RABBIT sidebands do not involve an intermediate resonance, e.g. SB18 is the interference between H17+IR and H19-IR pathways. By changing the APT-IR delay, the phase of each SB can be determined.

The phase delay of the interference of the sidebands has two contributions: the attosecond chirp or harmonic phase of the APT, and the photoionization phase (from the atomic phase). The phases of all of the sidebands can be seen to increase in a regular manner with harmonic order, except for the six-fold structure. The six-fold structure (trace A in (b)) has an additional $\pi/4$ phase shift not seen in the other panels. It has been reported that if ionization takes place through an intermediate resonant state, the resonance contributes an additional phase shift which is not seen in the higher sidebands [26], depending on the detuning. Our observation is consistent with the prediction that the six-fold structure arises from a resonant transition through the 3d state.

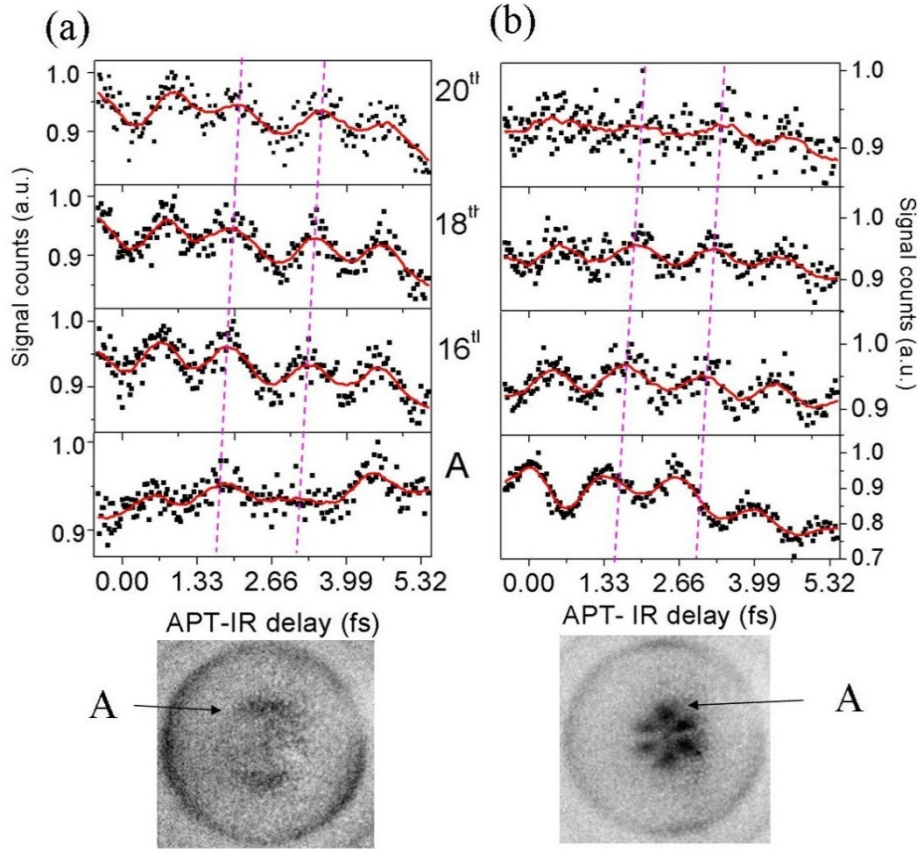


Fig. S4. Variation of photoelectron sideband signals as a function of the delay between the attosecond pulse train (APT) and the IR pulse for the case when (a) the a broad ring structure appears at low energy and (b) the six-fold structure appears, respectively. The 4 panels correspond to (top to bottom) RABBIT sidebands SB20, SB18, SB16 and the central feature A. The square data points are obtained by slicing the velocity map image along the laser polarization axis (vertical). The red lines are obtained by a 15 point running average. The corresponding VMI images are shown at the bottom for one delay. For the data points labeled as A, we take the signal counts at the radius corresponding to (a) the low-energy ring structure and (b) the low-energy six-fold structure, respectively. The magenta dotted lines represent the group delay of the attosecond pulse train. The phase of feature A in (b) is shifted relative to the RABBIT sidebands due to the phase shift caused by the 3d resonance.

3. Stark Shift of 3d State

The experiment shows that in our two-color XUV+IR experiment the final state for photoionization of neon is composed primarily of $m=0$ components. The initial 2p state also contains $m=+1$ and $m=-1$ components. Here we show that the Stark shift of the 3p resonant state can depend on the value of m .

Calculations were performed with a 3D TDSE solver [30] that has been shown to accurately reproduce experimental results [31]. An accurate effective potential is available for argon, but not for neon. Therefore the calculations presented below apply to argon. We use these calculations to support the plausibility of our argumentation the occurrence of m -dependent Stark shifts, but further calculations will be required to verify the case of neon.

The results are obtained from two-color calculations where overlapping XUV and IR pulses are prepared as follows. The XUV pulse is 150 cycles long (in order to get a reasonably narrow bandwidth) with a sine-squared envelope, and with a maximum field strength low enough ($6e-4$ a.u.) so that two-photon excitation is virtually absent in the calculation. The IR field is a pulse that is 18 cycles long, and that has a constant amplitude except for a half-cycle turn-on and turn-off, thus making sure that the XUV field always sees the same IR intensity.

The calculations start in the ground state of Ar, using either $m=0$ or $m=1$. Calculations were performed, where for a given IR field strength (varied between 0.0005 a.u. and 0.01 a.u.) we calculated the photoelectron spectrum as a function of XUV frequency. In all, a few thousand runs of the TDSE code were made.

There are two ways that the role of resonances shows up in these calculations. (1) When the XUV hits a resonance it leads to an increase of the photoelectron yield – this allows to determine the AC Stark-shifted energy of Rydberg states that show up in the calculation. (2) The photoelectron peaks that the calculation produces result from one- or two-photon ionization of resonances that have been prepared by the XUV, hence the observed photoelectron energy also allows an estimate of the AC Stark-shifted Rydberg energies. We observe a good consistency between these two methods of determining the AC Stark shift.

Figure S5 shows a typical example of a computational series for a given IR field strength, both for $m=0$ (top) and $m=1$ (bottom). Note the 4-order-of-magnitude intensity scale. The branch starting at $\omega_{xuv} = 0.53$ a.u. corresponds to ionization by one XUV-photon and one IR-photon, whereas for $\omega_{xuv} = 0.58$ a.u.

ionization by a single XUV photon becomes possible ($IP = 0.58135$ a.u.). A comparison of the top and bottom part of the Figure 1 immediately shows that there are significant differences between $m=0$ and $m=1$. In particular, the different location of some of the resonances (leading to regions of enhanced intensity in the photoelectron spectrum) stands out.

As a next step, we determine the precise location of the resonances in a series of figures like Figure S5 by interpolation, and as a function of the IR field strength. This leads to the results shown in Figure S6. The location of the observed resonances is shown for $m=0$ and $m=1$ as a function of IR field strength. If the levels would be purely ponderomotively shifted, all lines should evolve in the same manner as a function of the IR intensity, which is clearly not the case. Towards zero field, three resonances stand out, which correspond to the excitation of 4d, 5d and 6d intermediate resonances of argon.

Figure S5 shows that the number of photoelectrons produced depends on the photon energy and the magnetic quantum number. For example if the XUV is tuned to 0.552 a.u., the 2-photon signal (giving a kinetic energy around 0.02 a.u.) is an order of magnitude greater for $m=0$ than for $m=1$. This is also true for the 1-photon direct photoionization that gives electron kinetic energies around 0.08 a.u.

This calculation shows that it is plausible that only the $m=0$ component of the initial atomic state is selected, by tuning the intermediate resonant state by a combination of IR intensity and XUV frequency.

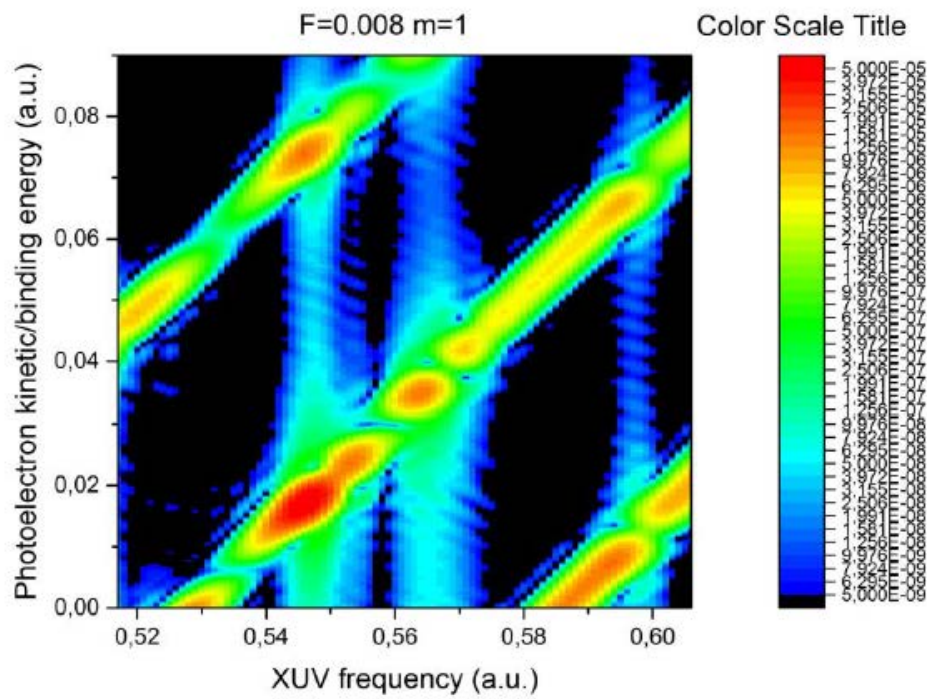
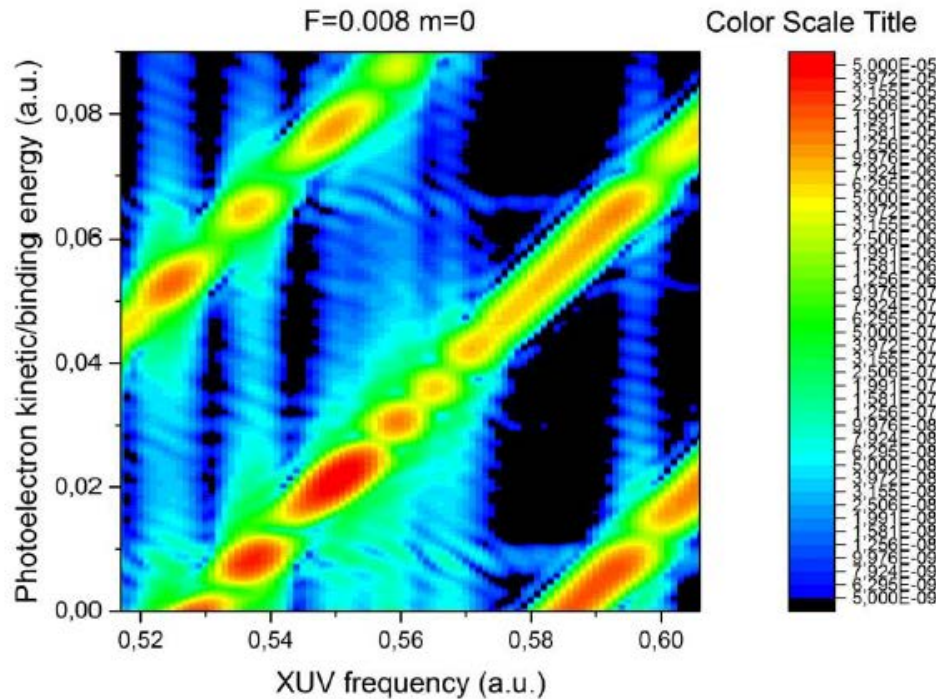


Figure S5: Calculated photoelectron kinetic energy distributions following XUV+IR ionization of Ar in the presence of a flat-top IR field with an amplitude of 0.008 a.u., for $m=0$ (top) and $m=1$ (bottom). The XUV frequency is varied across the horizontal axis. See text for further details on the pulses.

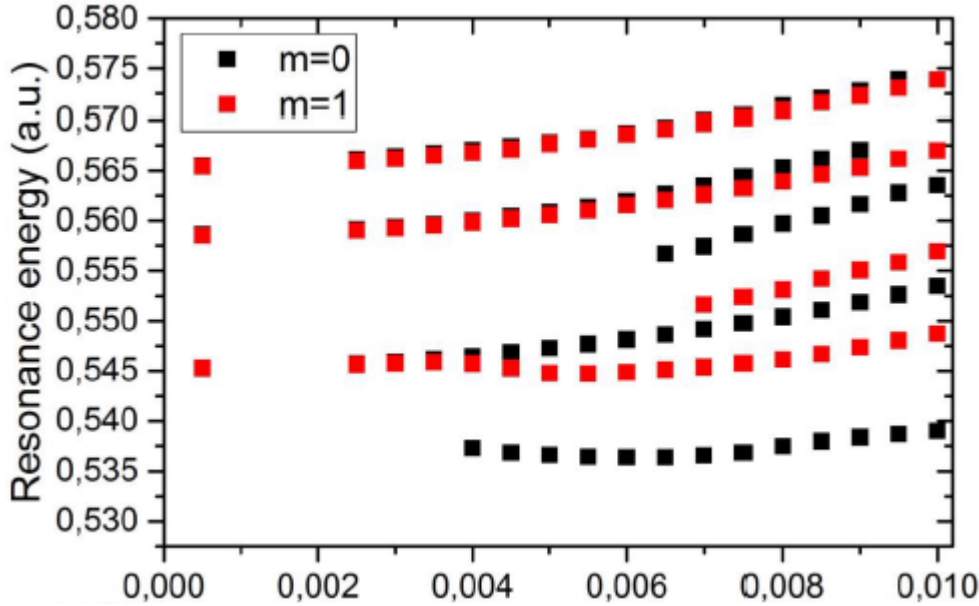


Figure S6: Resonances in XUV+IR ionization of Ar in the presence of a flat-top IR field for $m=0$ (black symbols) and $m=1$ (red symbols), as a function of the IR field strength. The figure shows the location of the resonances in the calculation. Clear differences between the $m=0$ and $m=1$ Stark shifts can be seen.

4. Fitting of Amplitudes and Phases of Partial Waves

The experiment recorded a series of VMI photoelectron images as a function of XUV-IR delay τ . A linear shading correction of 10% was applied across all images to compensate for spatial variation in detector efficiency, and the time base was linearized from glass plate tilt angle to time delay. The VMI data were binned into 8° angular sectors and integrated radially to give the angular distributions shown in Fig. 4(a) of the main text. The experimental image was then fit to a mathematical model composed of all possible partial wave contributions. The angular part of the continuum wave function was written as

$$\begin{aligned} \psi(\theta, \phi) = & A_s Y_0^0 + A_d e^{i\phi_d} Y_2^0 + (A_{p13} e^{i\phi_{p13}} Y_1^0 + A_{f13} e^{i\phi_{f13}} Y_3^0) e^{i\omega_0 \tau} \\ & + (A_{p15} e^{i\phi_{p15}} Y_1^0 + A_{f15} e^{i\phi_{f15}} Y_3^0) e^{-i\omega_0 \tau} \end{aligned}$$

The partial wave components were summed coherently, squared, and projected onto a 2D plane, then binned into angular sectors in the same way as the experimental results. This model produced an image such as that shown in Fig. 4(b) of the manuscript. The experimental image was subtracted from the model image point-by-point, and the difference-squared was summed. This resulted in a goodness-of-fit parameter in a least-squares sense. The parameters in the model were varied to create a global optimum fit of the parameters.

In order to ensure that a global as opposed to local minimum of the least-squares difference was obtained, a genetic algorithm was employed, the Particle Swarm Optimization (PSO) [32]. A set of 10^7 random initial conditions for the 12 parameters of the model (6 amplitudes, 5 phases, and ω_0) were evaluated. The swarm of parameters then moved towards the best global solution, but at the same time it randomly explored other parameters. After 100 iterations (36 hours on a 16-core processor) the optimum solution was found.

4.1 Experiment with H14 Alone

A separate experiment was performed in which even and odd harmonics were generated in the HHG medium, but no IR field was present. The low kinetic energy electrons were then produced solely by H14, and only s and d partial waves are possible. The result shown in Fig. S7 is consistent with the results of the full 12-parameter fit, except that the relative phase between the s- and d-waves is slightly different. The H14-alone experiment was performed under slightly different experimental conditions than the full scan described in the main text, but the reasonable agreement gives additional confidence in the results.

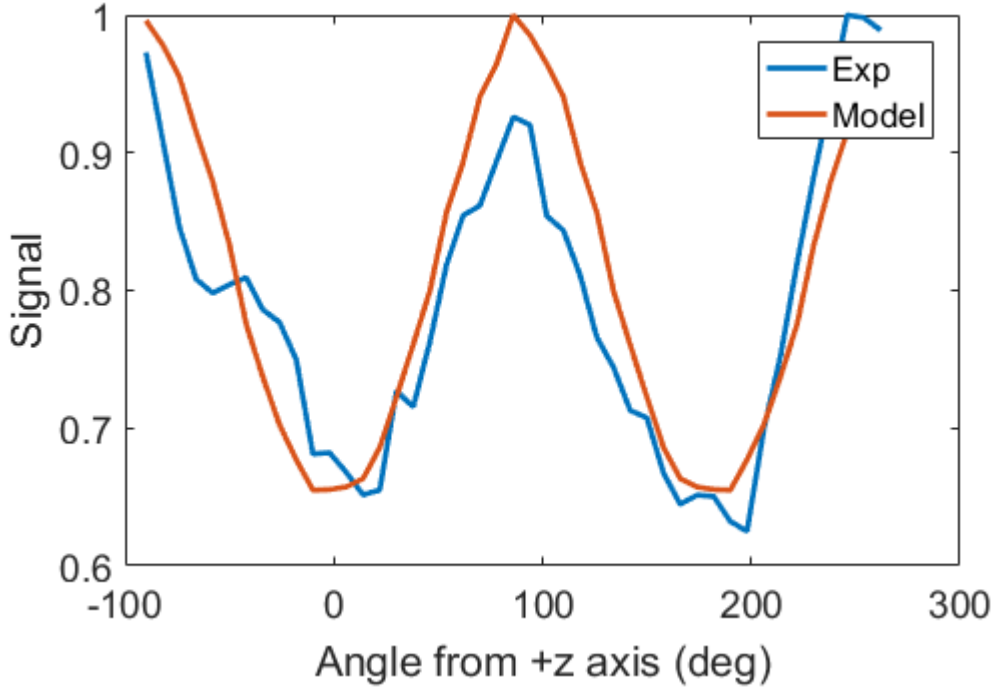


Figure S7. Blue trace: experimental angular distribution of the low energy component when H14 is present, in the absence of the IR probe field. The red trace is the model fit using two partial waves: $A_s=0.8290$, $\phi_s = 0$, $A_d=0.1030$, $\phi_d = 2.5$. The model fit determined in Table 1 had $A_s=0.8290$, $\phi_s = 0$, $A_d=0.1030$, $\phi_d = 1.5747$. The only difference is the phase of the d partial wave which differs by 0.93 radians. The model curve is jagged because the model photoelectron distribution was projected onto the same pixelated surface as the experimental image.

4.2 Experiment with No H14

We can also compare the model results to the VMI image shown in Fig. 1(a) in the main text. The image shown there was taken without even harmonics, and included only p- and f-partial waves resulting from 2-photon processes. In comparison to the VMI projections in Fig. 2 of the main text, it can be seen that a pure f-wave has more intense lobes at 0 and 180 degrees, whereas in Fig. 1(a) the lobes have almost equal intensity. It is the weak coherent contribution of p-waves that serves to make all lobes equal.

We take the model predictions from Table 1 for the 4 p- and f-wave components to generate a simulated VMI image. That image is then processed in the same way as the experimental VMI images, to give an angular distribution. The comparison is shown in Fig. S8. It is seen that the model parameters give almost equal intensity to all 6 lobes, in agreement with the experiment.

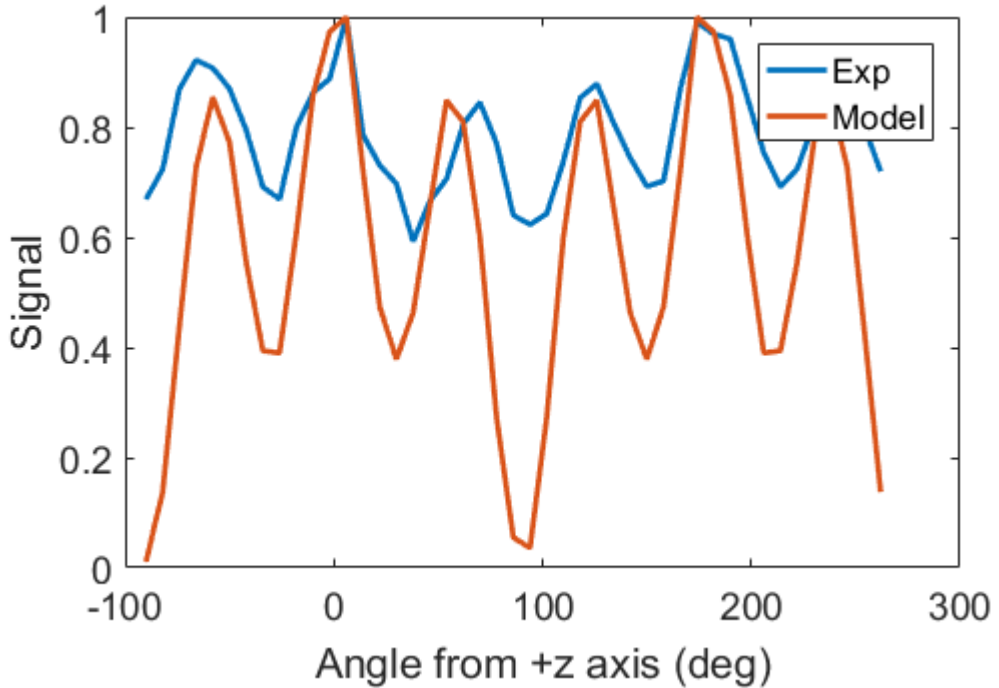


Figure S8. Comparison of the 6-fold structure in modelled and experimental VMI images recorded in the absence of the 400 nm driving field (i.e. no H14 present). The experimental image is shown in Fig. 1(a) of the main text. The model parameters of the 4 partial waves (p and d) were taken from Table 1 of the main text. Without the p-wave contribution, the lobes at 0 and 180 degrees (parallel to the polarization axis) would be much stronger than measured in the experiment. The p-wave contribution serves to make all 6 lobes approximately equal in intensity, as observed.

References and Notes

1. H. Wimmel, *Quantum Physics and Observed Reality: A Critical Interpretation of Quantum Mechanics* (World Scientific, Singapore, 1992).
2. A. S. Stodolna, A. Rouzée, F. Lépine, S. Cohen, F. Robicheaux, A. Gijsbertsen, J. H. Jungmann, C. Bordas, M. J. J. Vrakking, Hydrogen atoms under magnification: Direct observation of the nodal structure of Stark states. *Phys. Rev. Lett.* **110**, 213001 (2013).
[doi:10.1103/PhysRevLett.110.213001](https://doi.org/10.1103/PhysRevLett.110.213001) [Medline](#)
3. H. Niikura, F. Légaré, R. Hasbani, A. D. Bandrauk, M. Y. Ivanov, D. M. Villeneuve, P. B. Corkum, Sub-laser-cycle electron pulses for probing molecular dynamics. *Nature* **417**, 917–922 (2002). [doi:10.1038/nature00787](https://doi.org/10.1038/nature00787) [Medline](#)
4. J. Itatani, J. Levesque, D. Zeidler, H. Niikura, H. Pépin, J.-C. Kieffer, P. B. Corkum, D. M. Villeneuve, Tomographic imaging of molecular orbitals. *Nature* **432**, 867–871 (2004).
[doi:10.1038/nature03183](https://doi.org/10.1038/nature03183) [Medline](#)
5. S. Haessler, J. Caillat, W. Boutu, C. Giovanetti-Teixeira, T. Ruchon, T. Auguste, Z. Diveki, P. Breger, A. Maquet, B. Carré, R. Taïeb, P. Salières, Attosecond imaging of molecular electronic wavepackets. *Nat. Phys.* **6**, 200–206 (2010). [doi:10.1038/nphys1511](https://doi.org/10.1038/nphys1511)
6. P. M. Kraus, B. Mignolet, D. Baykusheva, A. Rupenyan, L. Horný, E. F. Penka, G. Grassi, O. I. Tolstikhin, J. Schneider, F. Jensen, L. B. Madsen, A. D. Bandrauk, F. Remacle, H. J. Wörner, Measurement and laser control of attosecond charge migration in ionized iodoacetylene. *Science* **350**, 790–795 (2015). [doi:10.1126/science.aab2160](https://doi.org/10.1126/science.aab2160) [Medline](#)
7. M. Meckel, D. Comtois, D. Zeidler, A. Staudte, D. Pavičić, H. C. Bandulet, H. Pépin, J. C. Kieffer, R. Dörner, D. M. Villeneuve, P. B. Corkum, Laser-induced electron tunneling and diffraction. *Science* **320**, 1478–1482 (2008). [doi:10.1126/science.1157980](https://doi.org/10.1126/science.1157980) [Medline](#)
8. M. Meckel, A. Staudte, S. Patchkovskii, D. M. Villeneuve, P. B. Corkum, R. Dörner, M. Spanner, Signatures of the continuum electron phase in molecular strong-field photoelectron holography. *Nat. Phys.* **10**, 594–600 (2014). [doi:10.1038/nphys3010](https://doi.org/10.1038/nphys3010)
9. D. Ray, B. Ulrich, I. Bocharova, C. Maharjan, P. Ranitovic, B. Gramkow, M. Magrakvelidze, S. De, I. V. Litvinyuk, A. T. Le, T. Morishita, C. D. Lin, G. G. Paulus, C. L. Cocke, Large-angle electron diffraction structure in laser-induced rescattering from rare gases. *Phys. Rev. Lett.* **100**, 143002 (2008). [doi:10.1103/PhysRevLett.100.143002](https://doi.org/10.1103/PhysRevLett.100.143002) [Medline](#)
10. V. Gruson, L. Barreau, Á. Jiménez-Galan, F. Risoud, J. Caillat, A. Maquet, B. Carré, F. Lepetit, J.-F. Hergott, T. Ruchon, L. Argenti, R. Taïeb, F. Martín, P. Salières, Attosecond

dynamics through a Fano resonance: Monitoring the birth of a photoelectron. *Science* **354**, 734–738 (2016). [doi:10.1126/science.aah5188](https://doi.org/10.1126/science.aah5188) [Medline](#)

11. S. Haessler, B. Fabre, J. Higuet, J. Caillat, T. Ruchon, P. Breger, B. Carré, E. Constant, A. Maquet, E. Mével, P. Salières, R. Taïeb, Y. Mairesse, Phase-resolved attosecond near-threshold photoionization of molecular nitrogen. *Phys. Rev. A* **80**, 011404 (2009). [doi:10.1103/PhysRevA.80.011404](https://doi.org/10.1103/PhysRevA.80.011404)
12. K. T. Kim, D. H. Ko, J. Park, N. N. Choi, C. M. Kim, K. L. Ishikawa, J. Lee, C. H. Nam, Amplitude and phase reconstruction of electron wave packets for probing ultrafast photoionization dynamics. *Phys. Rev. Lett.* **108**, 093001 (2012). [doi:10.1103/PhysRevLett.108.093001](https://doi.org/10.1103/PhysRevLett.108.093001) [Medline](#)
13. G. Laurent, W. Cao, H. Li, Z. Wang, I. Ben-Itzhak, C. L. Cocke, Attosecond control of orbital parity mix interferences and the relative phase of even and odd harmonics in an attosecond pulse train. *Phys. Rev. Lett.* **109**, 083001 (2012). [doi:10.1103/PhysRevLett.109.083001](https://doi.org/10.1103/PhysRevLett.109.083001) [Medline](#)
14. J. Mauritsson, T. Remetter, M. Swoboda, K. Klünder, A. L’Huillier, K. J. Schafer, O. Ghafur, F. Kelkensberg, W. Siu, P. Johnsson, M. J. J. Vrakking, I. Znakovskaya, T. Uphues, S. Zherebtsov, M. F. Kling, F. Lépine, E. Benedetti, F. Ferrari, G. Sansone, M. Nisoli, Attosecond electron spectroscopy using a novel interferometric pump-probe technique. *Phys. Rev. Lett.* **105**, 053001 (2010). [doi:10.1103/PhysRevLett.105.053001](https://doi.org/10.1103/PhysRevLett.105.053001) [Medline](#)
15. T. Remetter, P. Johnsson, J. Mauritsson, K. Varjú, Y. Ni, F. Lépine, E. Gustafsson, M. Kling, J. Khan, R. López-Martens, K. J. Schafer, M. J. J. Vrakking, A. L’Huillier, Attosecond electron wave packet interferometry. *Nat. Phys.* **2**, 323–326 (2006). [doi:10.1038/nphys290](https://doi.org/10.1038/nphys290)
16. A. Rouzée, A. G. Harvey, F. Kelkensberg, D. Brambila, W. K. Siu, G. Gademann, O. Smirnova, M. J. J. Vrakking, Imaging the electronic structure of valence orbitals in the XUV ionization of aligned molecules. *J. Phys. At. Mol. Opt. Phys.* **47**, 124017 (2014). [doi:10.1088/0953-4075/47/12/124017](https://doi.org/10.1088/0953-4075/47/12/124017)
17. J. Cooper, R. N. Zare, Angular distribution of photoelectrons. *J. Chem. Phys.* **48**, 942–943 (1968). [doi:10.1063/1.1668742](https://doi.org/10.1063/1.1668742)
18. J. Cooper, R. N. Zare, “Photoelectron angular distributions,” in *Atomic Collision Processes*, G. Geltman, K. T. Mahanthappa, W. E. Brittin, Eds. (Lectures in Theoretical Physics, Gordon and Breach, 1969), vol. XIc, pp. 317–337.

19. Y.-Y. Yin, C. Chen, D. S. Elliott, A. V. Smith, Asymmetric photoelectron angular distributions from interfering photoionization processes. *Phys. Rev. Lett.* **69**, 2353–2356 (1992).
[doi:10.1103/PhysRevLett.69.2353](https://doi.org/10.1103/PhysRevLett.69.2353) [Medline](#)
20. U. Becker, Complete photoionisation experiments. *J. Electron Spectrosc. Relat. Phenom.* **96**, 105–115 (1998). [doi:10.1016/S0368-2048\(98\)00226-6](https://doi.org/10.1016/S0368-2048(98)00226-6)
21. J. C. Hansen, J. A. Duncanson, R.-L. Chien, R. S. Berry, Angular distributions of $3p0^2 P_{\frac{3}{2}}$ photoelectrons from resonant two-photon ionization of sodium through the intermediate state. *Phys. Rev. A* **21**, 222–233 (1980). [doi:10.1103/PhysRevA.21.222](https://doi.org/10.1103/PhysRevA.21.222)
22. K. L. Reid, Photoelectron angular distributions. *Annu. Rev. Phys. Chem.* **54**, 397–424 (2003).
[doi:10.1146/annurev.physchem.54.011002.103814](https://doi.org/10.1146/annurev.physchem.54.011002.103814) [Medline](#)
23. A. T. J. B. Eppink, D. H. Parker, Velocity map imaging of ions and electrons using electrostatic lenses: Application in photoelectron and photofragment ion imaging of molecular oxygen. *Rev. Sci. Instrum.* **68**, 3477–3484 (1997). [doi:10.1063/1.1148310](https://doi.org/10.1063/1.1148310)
24. N. Dudovich, O. Smirnova, J. Levesque, Y. Mairesse, M. Y. Ivanov, D. M. Villeneuve, P. B. Corkum, Measuring and controlling the birth of attosecond pulses. *Nat. Phys.* **2**, 781–786 (2006). [doi:10.1038/nphys434](https://doi.org/10.1038/nphys434)
25. E. B. Saloman, C. J. Sansonetti, Wavelengths, energy level classifications, and energy levels for the spectrum of neutral neon. *J. Phys. Chem. Ref. Data* **33**, 1113–1158 (2004).
[doi:10.1063/1.1797771](https://doi.org/10.1063/1.1797771)
26. M. Swoboda, T. Fordell, K. Klünder, J. M. Dahlström, M. Miranda, C. Buth, K. J. Schafer, J. Mauritsson, A. L’Huillier, M. Gisselbrecht, Phase measurement of resonant two-photon ionization in helium. *Phys. Rev. Lett.* **104**, 103003 (2010).
[doi:10.1103/PhysRevLett.104.103003](https://doi.org/10.1103/PhysRevLett.104.103003) [Medline](#)
27. N. Dudovich, D. Oron, Y. Silberberg, Coherent transient enhancement of optically induced resonant transitions. *Phys. Rev. Lett.* **88**, 123004 (2002).
[doi:10.1103/PhysRevLett.88.123004](https://doi.org/10.1103/PhysRevLett.88.123004) [Medline](#)
28. P. M. Paul, E. S. Toma, P. Breger, G. Mullot, F. Augé, P. Balcou, H. G. Muller, P. Agostini, Observation of a train of attosecond pulses from high harmonic generation. *Science* **292**, 1689–1692 (2001). [doi:10.1126/science.1059413](https://doi.org/10.1126/science.1059413) [Medline](#)
29. H. G. Muller, Reconstruction of attosecond harmonic beating by interference of two-photon transitions. *Appl. Phys. B* **74**, s17–s21 (2014). [doi:10.1007/s00340-002-0894-8](https://doi.org/10.1007/s00340-002-0894-8)

30. H. G. Muller, An efficient propagation scheme for the time-dependent Schrödinger equation in the velocity gauge. *Laser Phys.* **9**, 138–148 (1999).
31. M. J. Nandor, M. A. Walker, L. D. Van Woerkom, H. G. Muller, Detailed comparison of above-threshold-ionization spectra from accurate numerical integrations and high-resolution measurements. *Phys. Rev. A* **60**, R1771–R1774 (1999).
[doi:10.1103/PhysRevA.60.R1771](https://doi.org/10.1103/PhysRevA.60.R1771)
32. J. Kennedy, R. Eberhart, “Particle swarm optimization,” in the *Institute of Electrical and Electronics Engineers (IEEE) International Conference on Neural Networks Proceedings* (IEEE, 1995), vol. 4, pp. 1942–1948.